INTERNATIONAL JOURNAL FOR NUMERICAL METHODS IN FLUIDS
Int. J. Numer. Meth. Fluids 2007; **54**:29–46
Published online 30 November 2006 in Wiley InterScience (www.interscience.wiley.com). DOI: 10.1002/fld.1390

An enhanced polygonal finite-volume method for unstructured hybrid meshes

Hyung Taek Ahn[†,*] and Graham F. Carey

Institute for Computational Engineering and Sciences, The University of Texas at Austin, Austin, TX 78712, U.S.A.

SUMMARY

Irregular hybrid meshes may excessively distort the node-dual finite-volume discretization. A new scheme is formulated that uses a different type of polygonal control volume. Superior stability of the polygonal scheme over the conventional node-dual scheme is demonstrated on representative irregular hybrid meshes for incompressible viscous flow past a circular cylinder. Copyright © 2006 John Wiley & Sons, Ltd.

Received 25 January 2006; Revised 19 September 2006; Accepted 20 September 2006

KEY WORDS: mesh distortion; polygonal finite volume; node-dual finite volume; unstructured hybrid mesh

1. INTRODUCTION

Unstructured hybrid meshes are increasingly being used in complex engineering and science applications, since they afford the opportunity to fit complex geometry and grade meshes for more efficient accurate simulations. One of the difficulties encountered with such meshes is, however, the degradation in the quality of an approximate solution that may occur because of mesh distortion and poor mesh transition [1]. These mesh quality problems for unstructured finite element and finite-volume schemes usually are seen in the context of the primary hybrid mesh that is comprised of simplices, tensor product or similar basic cells. It is also an issue for simulations on the associated dual meshes. For example, one may need to deal with slender sliver simplices and skew quadrilaterals in a 2D hybrid mesh or irregular polygons in the associated dual Voronoi diagram [2].

In the case of the primary hybrid mesh, there are a number of strategies for mesh quality improvement that are being studied and implemented. Most of these schemes involve moving the

*Correspondence to: Hyung Taek Ahn, Theoretical Division, Group T-7, MS-B284, Los Alamos National Laboratory, Los Alamos, NM 87545, U.S.A.
†E-mail: htahn@lanl.gov

nodes of the primary hybrid mesh to improve some measure of cell quality and thereby enhance robust simulations on the improved hybrid mesh [3–5]. There has been much less work on the associated *dual* mesh problem that is the focus of the present work. Here, we develop and test a polygonal approach and compare results with those of a standard finite-volume node-based dual scheme.

Polygonal mesh constructions have been used previously [6, 7]: Wright and Smith [6] introduced a polygonal interpretation of the node-dual approach on 2D hybrid meshes for applications with a pressure-correction incompressible Navier–Stokes solver. Their approach (in fact, a node-dual scheme) is restricted due to specification of velocity variables at nodes and pressure at cell centres of the base mesh. Loubère and Shashkov [7] use a mimetic finite different method and subdivide the a polygonal cell into multiple quadrilateral subcells, having variables associated with polygonal cells, nodes and subcells. The distinctions of the present polygonal approach are: (i) independence from the base hybrid mesh in terms of variable location and flux computation and (ii) a simpler data structure that uses neither the staggered approach nor subdivision of polygonal cells.

The main problem considered here in the mesh sensitivity tests is incompressible viscous flow around a circular cylinder. This is an important problem class of wide interest and is therefore an appropriate test for this comparison study. Other studies for the familiar driven cavity problem are also included to illustrate these mesh effects in the context of another standard test problem.

The present paper is structured as follows: in the first section we briefly outline the conservation equations and solution scheme for the viscous flow problem to be simulated in tests of the new polygonal volume scheme. In the next two sections we describe the node-dual and the new polygonal dual schemes. Details of the viscous flux and advective flux treatment are given. These dual schemes are then compared for impulsively started viscous incompressible flow past a cylinder and lid-driven cavity problem. Of particular interest are the effects of mesh distortion and hybrid mesh transition. A study of mesh effects for the driven cavity problem is included to further illustrate some of the key points. The main observations are summarized in the concluding remarks.

2. VISCOUS FLOW TEST PROBLEM

For completeness and to facilitate possible future comparison studies by other researchers, we first summarize the governing equations and solution method.

2.1. Governing equations

The conservation laws of mass and momentum for an arbitrary closed control volume V with boundary S in integral form can be expressed as

$$\frac{\mathrm{d}}{\mathrm{d}t}\int_V \rho \,\mathrm{d}V + \int_S \rho \mathbf{V}\cdot\hat{\mathbf{n}}\,\mathrm{d}S = 0 \tag{1}$$

$$\frac{\mathrm{d}}{\mathrm{d}t}\int_V \rho \mathbf{V}\,\mathrm{d}V + \int_S \rho \mathbf{V}\mathbf{V}\cdot\hat{\mathbf{n}}\,\mathrm{d}S = \int_S \boldsymbol{\sigma}\cdot\hat{\mathbf{n}}\,\mathrm{d}S \tag{2}$$

where $\mathbf{V}^{\mathrm{T}}$ is the velocity vector, density ρ is constant for incompressible flow, and $\hat{\mathbf{n}}$ is the unit outward normal vector for the control volume. The stress tensor $\boldsymbol{\sigma}$ is composed of the normal

DOI: 10.1002/fld

stress representing hydrostatic pressure p and the shear stress τ_{ij}.

$$\sigma_{ij} = -p\delta_{ij} + \tau_{ij}$$

For a Newtonian fluid, the shear stress tensor is defined by

$$\tau_{ij} = \mu\left(\frac{\partial u_i}{\partial x_j} + \frac{\partial u_j}{\partial x_i}\right)$$

where μ is dynamic viscosity, and u_i is the ith component of the velocity vector.

Introducing a characteristic length scale and free stream reference quantities, the governing equations are non-dimensionalized and written in system form as follows:

$$\frac{\mathrm{d}}{\mathrm{d}t}\int_V \mathbf{U}\,\mathrm{d}V + \int_S (\mathbf{F}_I\hat{\mathbf{i}} + \mathbf{G}_I\hat{\mathbf{j}})\cdot\hat{\mathbf{n}}\,\mathrm{d}S = \int_S (\mathbf{F}_V\hat{\mathbf{i}} + \mathbf{G}_V\hat{\mathbf{j}})\cdot\hat{\mathbf{n}}\,\mathrm{d}S \tag{3}$$

where $\mathbf{U}$ is the vector of conserved flow quantities, $\mathbf{F}_I\hat{\mathbf{i}}+\mathbf{G}_I\hat{\mathbf{j}}$ is the convective flux vector $\mathbf{F}_V\hat{\mathbf{i}}+\mathbf{G}_V\hat{\mathbf{j}}$ is the viscous flux vector and $\hat{\mathbf{n}}$ is the outward unit normal vector to V. For the 2D comparison studies considered later we have

$$\mathbf{U} = \begin{Bmatrix} 1 \\ u \\ v \end{Bmatrix}, \quad \mathbf{F}_I = \begin{Bmatrix} u \\ uu + p \\ vu \end{Bmatrix}, \quad \mathbf{G}_I = \begin{Bmatrix} v \\ uv \\ vv + p \end{Bmatrix}$$

$$\mathbf{F}_V = \frac{1}{Re}\begin{Bmatrix} 0 \\ 2\dfrac{\partial u}{\partial x} \\ \dfrac{\partial u}{\partial y} + \dfrac{\partial v}{\partial x} \end{Bmatrix}, \quad \mathbf{G}_V = \frac{1}{Re}\begin{Bmatrix} 0 \\ \dfrac{\partial v}{\partial x} + \dfrac{\partial u}{\partial y} \\ 2\dfrac{\partial v}{\partial y} \end{Bmatrix}$$

where $Re = U_\infty D/\nu$ is the Reynolds number and $\nu = \mu/\rho$ is the kinematic viscosity. In Figure 1, typical finite volumes constructed by a median node-dual scheme are sketched.

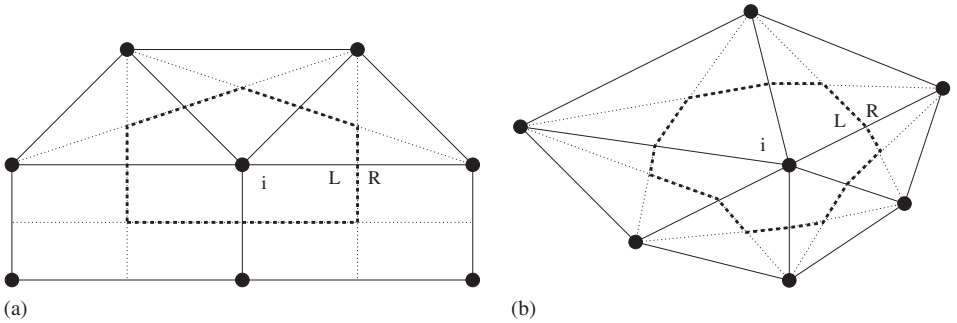

Figure 1. Node-duals in two dimensions constructed by median-dual scheme: (a) node-dual with mixed cells; and (b) node-dual with triangular cells.

DOI: 10.1002/fld

2.2. Time-accurate artificial compressibility method

An artificial compressibility approximation for time-accurate solution due to Belov [8] is used with the dual time-stepping algorithm of Jameson [9]:

$$\mathbf{P}\frac{\mathrm{d}}{\mathrm{d}t^*}\int_V \mathbf{Q}\,\mathrm{d}V + \frac{\mathrm{d}}{\mathrm{d}t}\int_V \mathbf{U}\,\mathrm{d}V + \int_S (\mathbf{F}_I\hat{\mathbf{i}} + \mathbf{G}_I\hat{\mathbf{j}})\cdot\hat{\mathbf{n}}\,\mathrm{d}S$$
$$= \int_S (\mathbf{F}_V\hat{\mathbf{i}} + \mathbf{G}_V\hat{\mathbf{j}})\cdot\hat{\mathbf{n}}\,\mathrm{d}S \tag{4}$$

A pseudo-time-derivative term (time-derivative with respect to pseudo-time, t^*) has been added here to both the continuity equation and the momentum equations. Hence, the continuity equation has a pseudo-time-derivative for pressure and the momentum equations have both true time-derivatives and the added pseudo-time-derivatives of the velocity components.

The vector $\mathbf{Q}$ in the above system contains the primitive solution variables, and $\mathbf{P}$ is a diagonal matrix containing the artificial compressibility parameter β which acts as a pre-conditioner for the continuity equation

$$\mathbf{P} = \begin{bmatrix} 1/\beta & 0 & 0 \\ 0 & 1 & 0 \\ 0 & 0 & 1 \end{bmatrix}, \quad \mathbf{Q} = \begin{Bmatrix} p \\ u \\ v \end{Bmatrix} \tag{5}$$

The artificial compressibility parameter β controls the speed of artificial pressure waves and also affects the overall convergence rate through the preconditioning. Depending on the preconditioning method needed, a more complex form of the preconditioning matrix can be constructed by making variable β a simple function of the local flow velocity [10, 11]. More recently, Malan *et al.* [12] included the viscous effect in the artificial compressibility parameter β, and Nithiarasu [13] presented the characteristic based split artificial compressibility method for a wide range of Reynold's numbers. The main idea of the variable β is to minimize the disparity of the eigenvalues by scaling the artificial speed of sound which is a function of β. However, numerous results have been reported that imply using a constant β is preferred [14–16]. Hence, a globally constant β in the orders of $O(1) \sim O(100)$ is used for the present work, and $\beta = 100$ is found to work best for the overall convergence in the cases considered here.

In Figure 1, typical finite-volumes constructed by a median node-dual scheme are sketched. In order to advance a time step from the current time t_n to the next time t_{n+1}, the unsteady residual (true time-derivative plus flux terms) is first constructed by discretizing the true time-derivative with the second-order implicit backward difference formula, and then the steady-state problem is solved in pseudo-time. Once the steady state in pseudo-time is reached, the solution has been advanced to the next time step.

3. NODE-DUAL FINITE-VOLUME SCHEME

3.1. Median-dual finite volume

A conservative, finite-volume discretization scheme can be constructed from Equation (3) by introducing a partition of non-overlapping control volumes and a suitable approximation scheme

DOI: 10.1002/fld

for derivatives. A standard approach is to construct a node-centred median-dual volume partition for spatial discretization with an edge-based algorithm for computing numerical fluxes [16, 17]. We present this as the base method for our comparison.

Velocity gradients on the control-volume edges are needed in the viscous term so we introduce an auxiliary edge-based control volume class and a computationally efficient algorithm for this calculation [16, 18]. The resulting algorithm is composed of a face-wise loop to evaluate the surface integrals of edge-duals followed by an edge-wise operation for the final computation of velocity gradients and viscous fluxes.

The dashed lines surrounding node i in Figure 1 define boundaries of node-centred median-dual control volumes for a representative hybrid mesh patch and triangular mesh patch, respectively. The dashed node-dual boundary of the control volume is constructed by connecting the corresponding edge midpoints in the primal mesh to centroids of the cells adjacent to these points. The symbols L and R in Figure 1 denote left and right sides of the node-dual boundary assuming counterclockwise traversal of the boundary with normal directed outward in the usual manner.

3.2. *Convective flux*

The convective flux approximation for the subregion corresponding to node-dual i can be expressed as

$$\oint_{S_i} (\mathbf{F}_I \mathbf{i} + \mathbf{G}_I \mathbf{j}) \cdot \mathbf{n} \, \mathrm{d}S \approx \sum_{j=1}^{J_i} (\mathscr{F})_j \Delta S_j \tag{6}$$

where $(\mathscr{F})_j = \mathbf{F}_I n_x + \mathbf{G}_I n_y$ is the numerical flux evaluated at the mid-point of edge j, J_i denotes the number of edges connected to node i and ΔS_j is the area of the node-dual boundary associated with edge j.

Instead of a central scheme with the additional artificial dissipation term, an upwind scheme is introduced to evaluate the numerical fluxes using Roe's approximate Riemann solver [19] with

$$\mathscr{F}_{\text{upwind}} = \tfrac{1}{2} (\mathscr{F}(\mathbf{Q}_\mathrm{L}) + \mathscr{F}(\mathbf{Q}_\mathrm{R})) + \tfrac{1}{2} \hat{\mathbf{A}}(\mathbf{Q}_\mathrm{R}, \mathbf{Q}_\mathrm{L})(\mathbf{Q}_\mathrm{L} - \mathbf{Q}_\mathrm{R}) \tag{7}$$

where $\mathscr{F}(\mathbf{Q}_\mathrm{L})$ and $\mathscr{F}(\mathbf{Q}_\mathrm{R})$ are the convective flux vectors from the solutions reconstructed on the left ($\mathbf{Q}_\mathrm{L}$) and right ($\mathbf{Q}_\mathrm{R}$) sides of the control-volume boundary. These solutions are reconstructed by using Taylor series expansions about the two end nodes corresponding to the edge mid-point where precomputation of nodal gradients of the solution is to be made. Matrix $\hat{\mathbf{A}}$ may be expressed in the form

$$\hat{\mathbf{A}} = \mathbf{R} \hat{\mathbf{\Lambda}} \mathbf{R}^{-1}$$

where the $\mathbf{R}$ is the right eigenvector matrix of the flux Jacobian, $\mathbf{R}^{-1}$ is its inverse, and $\hat{\mathbf{\Lambda}}$ is the diagonal matrix whose components are absolute values of the associated eigenvalues. Following Taylor and Whitfield [20], each component of the matrix $\hat{\mathbf{A}}$ is evaluated by arithmetic averaging of the left and right states. The eigensystem is non-singular as shown by Anderson *et al.* [21] in two dimensions, and by Kim [22] in three dimensions.

When a first-order upwind scheme is employed, the solutions on the left and right sides of the control-volume boundary are specified to be the solutions at the corresponding two end nodes on that primal mesh edge. This is effectively a zero order (constant approximation on the half interval) Taylor series result for expansion about the respective end nodes. For higher-order upwind schemes,

DOI: 10.1002/fld

these values at the control-volume boundary are reconstructed by using higher-order Taylor series expansions. Hence, for a second-order scheme we have

$$\mathbf{Q}_{\mathrm{L}} = \mathbf{Q}_i + \tfrac{1}{2}(\nabla \mathbf{Q})_i \cdot \Delta \mathbf{r}_{ij} \tag{8}$$

$$\mathbf{Q}_{\mathrm{R}} = \mathbf{Q}_j - \tfrac{1}{2}(\nabla \mathbf{Q})_j \cdot \Delta \mathbf{r}_{ij} \tag{9}$$

where $\Delta \mathbf{r}_{ij}$ is the distance vector from node i to j, and $\nabla \mathbf{Q}$ is the nodal gradient of the solution and is evaluated by a least-squares procedure [23] using Gram–Schmidt orthogonalization for QR decomposition. This Gram–Schmidt process allows precomputation of all the weights from the geometric information alone. Hence, the actual computation of the nodal gradients using the least-squares procedure can be implemented by a single loop over edges. For further details see Anderson and Bonhaus [23] and Haselbacher and Blazek [24], respectively, for application to two and three dimensions.

The surface integral formulation in Equation (6) implies accumulating contributions from edges of the control volume for each node. However, the actual implementation is edge-wise with positive contribution to the node inside and negative contribution to the node outside depending on the direction of edge traversal. This edge-wise algorithm does not require any information about cell topology, so the algorithm is especially suitable for general hybrid meshes such as those considered later.

3.3. Viscous flux

The gradients of velocity components need to be precomputed at each edge in order to evaluate the viscous fluxes through the control-volume boundaries. We use an auxiliary edge-dual finite-volume for this velocity gradient computation. This auxiliary edge-dual control volume is composed of neighbour cells sharing a common edge. Representative edge-dual regions encountered in hybrid meshes are shown in Figure 2.

The divergence theorem is applied in the interior of each finite-volume to yield corresponding surface integrals along edge-dual boundaries. For instance, the volume-averaged value of $\partial u/\partial x$ using an edge-dual can be expressed in this way as

$$\left(\frac{\partial u}{\partial x}\right)_{\mathrm{e}} = \frac{1}{V_{\mathrm{e}}} \oint_{\mathrm{e}} u n_x \, \mathrm{d}S \tag{10}$$

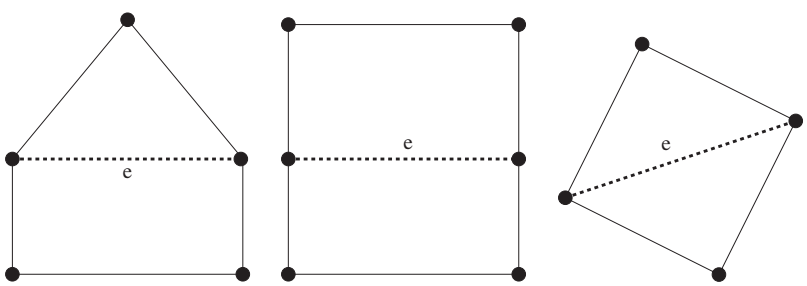

Figure 2. Edge-duals in two dimensions for computation of the first order spatial derivatives.

DOI: 10.1002/fld

where V_e is the volume of an edge-dual. The resulting surface integrals are approximated as described earlier. This edge-dual approach has been advocated by other researchers [25, 26] because it is less susceptible to numerical oscillations and yields more compact stencils than some other methods. Once the velocity gradients are computed at all edges, the same edge-wise operation is used for the viscous flux evaluation at node i as shown previously; that is, edge contributions to node i are accumulated using

$$\oint_{S_i} (\mathbf{F}_V \mathbf{i} + \mathbf{G}_V \mathbf{j}) \cdot \mathbf{n} \, \mathrm{d}S \approx \sum_{j=1}^{J_i} (\mathscr{F}_V)_j \Delta S_j \tag{11}$$

where $(\mathscr{F}_V)_j = \mathbf{F}_V n_x + \mathbf{G}_V n_y$ is the viscous flux evaluated at the edge j, J_i is number of edges connected to node i, and ΔS_j is the area of the node-dual boundary associated with the jth edge. This edge-wise operation for viscous flux evaluation can be combined with the second step of the algorithm which evaluates the velocity gradients.

4. POLYGONAL FINITE-VOLUME SCHEME

4.1. Cell quality

For regular smoothly graded meshes the node-dual (e.g. median-dual or centroid-dual) finite-volume scheme gives relatively good results. (For triangular 2D meshes, the median-dual scheme is equivalent to a Galerkin finite element method [17] so some of the same restrictions apply to mesh quality for this methodology.) More specifically, as the node-dual shape quality degrades, the solution quality will also deteriorate and local oscillations in the solution are promoted as seen later. The deterioration in the node-dual mesh for different primal mesh configurations is indicated in Figure 3.

One of the common problems for a node-dual scheme on an irregular mesh is that location of solution (nodal points) deviates significantly from the corresponding control volumes (node-duals). In such a case, the nodal solution may also deviate similarly from the average value for the cell around the node. Hence, the basic node-dual scheme with eccentric nodal locations inherently introduces errors in approximating a volume averaged solution.

Furthermore, if a median-dual scheme is employed, the control volume may easily become non-convex. If a cell has non-convex boundaries between its neighbours, the two neighbouring cells (sharing the non-convex boundary section) can be both an upstream-cell as well as a downstream-cell to each other. This can be a source of numerical error especially when an upwind scheme is employed [27].

We present two measures for quantifying the node-dual quality: (i) the eccentricity (departure) of the node from the centroid of the node-dual subregion and (ii) the non-convexity of node-dual with respect to its neighbours. The eccentricity for a cell around node i can be expressed as

$$\text{eccentricity}_i = \frac{\|\mathbf{r}_n - \mathbf{r}_c\|}{\sqrt{S_i/\pi}} \tag{12}$$

DOI: 10.1002/fld

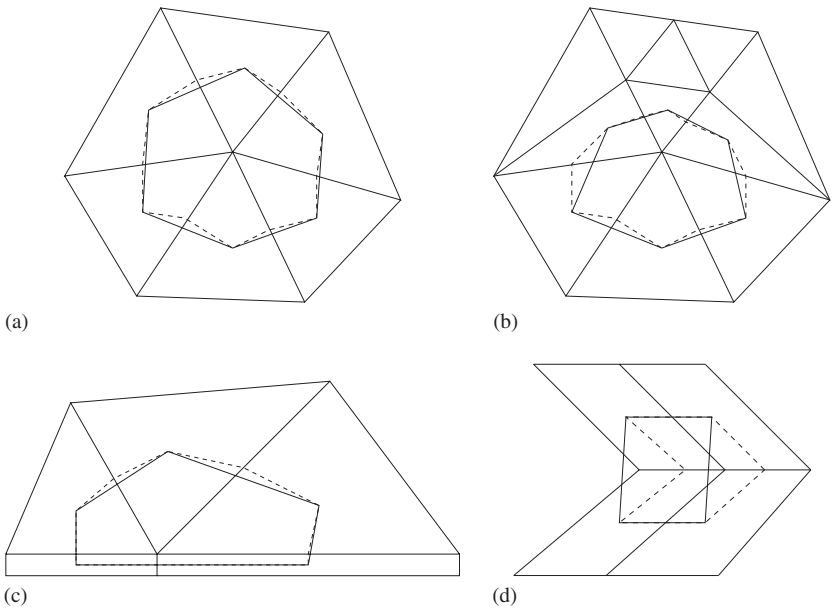

Figure 3. Mesh quality effect on node-dual finite-volume construction. Median-duals are delineated by dashed lines, and centroid-duals are represented with solid lines: (a) regular represents a smooth mesh; (b) irregular type 1 shows the smooth mesh with a refined cell; (c) irregular type 2 displays the hybrid mesh with discontinuous change of element size; and (d) irregular type 3 represents a distorted mesh with sharp angles.

where $\mathbf{r}_n$ and $\mathbf{r}_c$ are co-ordinates of node and node-dual centroid and S_i is the area of the control volume around node i. The non-convexity of a control volume can also be presented as

$$\text{non-convexity}_i = \frac{\sum_{j=1}^{J_i} |\min(\Delta S_{ij}, 0)|}{S_i} \tag{13}$$

where S_{ij} is the area of triangular region associated with edge ij as delineated in Figure 4, and J_i denotes the number of edges connected to node i. The idea of non-convexity of a control-volume boundary presented above is different from the definition of the convex hull [2]. We illustrate the point here for two neighbour cells.In the polygonal finite-volume approach to be presented next, the eccentricity is always zero because the solution variables are stored at the centroid of each polygonal cell. Furthermore, the inter-cell boundary is always convex because the inter-cell boundary is represented with a single straight line.

4.2. Polygonal volume approach

To avoid the above sensitivity in the node-dual scheme, we propose an alternative polygonal finite-volume approach. This polygonal control volume is constructed by connecting centroid-duals of the given mesh and the finite-volume scheme works as a cell-centred scheme with respect to the polygonal finite-volume.

DOI: 10.1002/fld

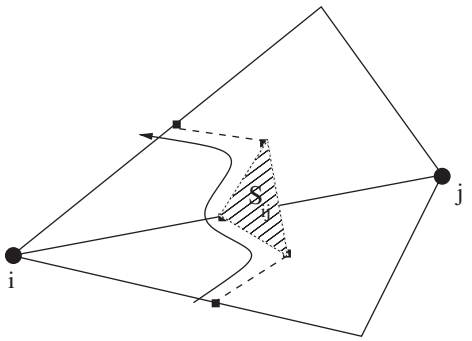

Figure 4. Non-convex inter-cell boundary. Dashed lines indicate the boundary of node-dual around node i. The non-convex volume fraction, S_{ij} (negative area), is delineated by the shaded region. A solid arrowed line indicates the path of the boundary of a control volume around node i.

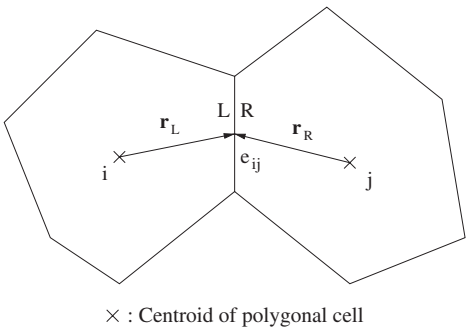

Figure 5. Convective flux computation with polygonal finite-volume scheme.

The convective flux computation with this polygon control volume is illustrated in Figure 5. The convective flux across the boundary of this control volume is again computed using the Roe's flux-difference splitting, as written in Equation (7). For each polygonal cell, all solution variables are stored at the centroid, and solutions are reconstructed at the boundary of the polygonal finite-volumes.

As shown in Figure 5, the convective flux on a segment shared by adjacent control volumes is computed using the reconstructed solution at the common polygonal boundary (e_{ij}) between control volume cell i and cell j. The contributions on the left (L) and right (R) sides of the boundary corresponding to Equations (8) and (9) become

$$\mathbf{Q}_L = \mathbf{Q}_i + (\nabla \mathbf{Q})_i \cdot \mathbf{r}_L \tag{14}$$

$$\mathbf{Q}_R = \mathbf{Q}_j + (\nabla \mathbf{Q})_j \cdot \mathbf{r}_R \tag{15}$$

where gradient $\nabla \mathbf{Q}$ of the solution is computed as before by least squares using adjacent neighbouring polygonal cells.

Viscous flux computation for the polygonal volume is illustrated in Figure 6. The main question here is how to compute the velocity gradient at a control-volume boundary. We again apply an

DOI: 10.1002/fld

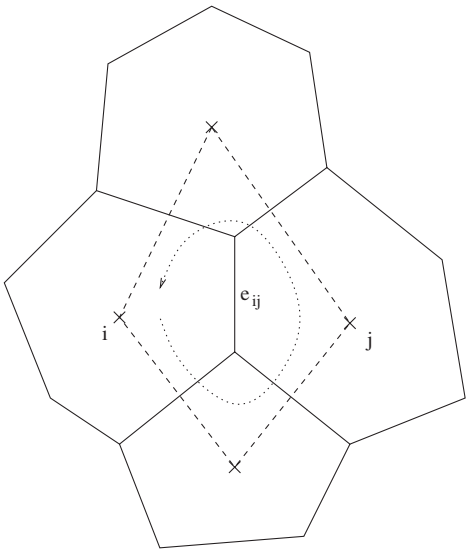

Figure 6. Velocity gradient computation using cells around common edge (e_{ij}). Dashed lines indicate secondary finite volume (edge-dual, V_e) for velocity gradient computation and dotted arrowed line indicates the direction of boundary integral.

auxiliary finite-volume strategy as in the node-dual scheme and compute the gradient of velocity by volume averaging as in Equation (10). The difference in the velocity gradient computation is that for a polygonal scheme the edge dual (V_e) is not constructed using the primal mesh node points but instead uses centroids of neighbouring polygons.

4.3. Extension to 3D

The conceptual extension to 3D polyhedral finite-volume methods is clear: 3D requires definition of a corresponding polyhedral control-volume based on a given hybrid mesh. However, there is an additional level of complexity. The main new difficulty is that there is no clear definition of *planar* representation of inter-cell boundary. For example, in a node-dual approach [16, 28], as shown in Figure 7(b), the node-dual is constructed with multiple patches of quadrilateral faces. For a given edge, these quadrilateral patches are gathered from neighbour cells to obtain the inter-cell boundary. This inter-cell boundary is not necessarily co-planar nor each of the quadrilateral patches (except for patches from tetrahedral neighbour cells). Hence, these non-planar inter-cell boundaries eventually result in non-convex control volumes.

In the polyhedral approach, as shown in Figure 7(c), a unique polygonal plane can be defined for each edge and the polygonal plane represents the inter-cell boundary. The planar polygonal inter-cell boundary is constructed in two steps: first a least-squares approach is computed using the quadrilateral paches from the node-dual to construct a planar representation of this inter-cell boundary, and in the second step the intersections of the planar inter-cell boundary are computed for the polygonal representation of the inter-cell boundary. Once the polyhedral control volume is defined, the flux computation can again be performed as described as in Figure 5. Implementation of the 3D polyhedral method for flow calculations on hybrid meshes is under development.

DOI: 10.1002/fld

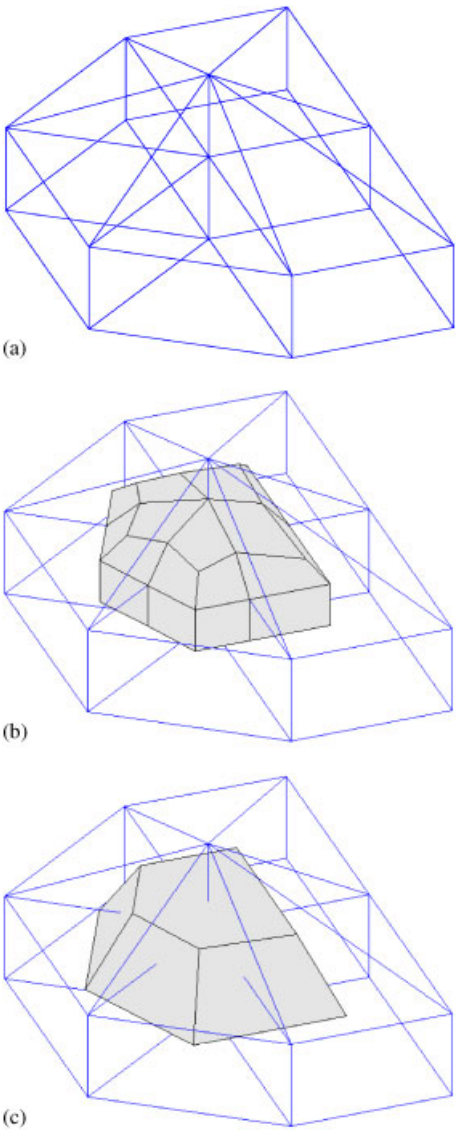

Figure 7. Polyhedral and node-dual finite volume based on a 3D hybrid mesh: (a) 3D hybrid mesh; (b) node-dual control volume; and (c) polyhedral control volume.

5. RESULTS

A comparative study of node-dual and polygonal schemes is presented here for three cases: (1) a hybrid mesh with random local cell distortions in a subregion; (2) a hybrid mesh with an abrupt mesh transition at the mesh-type interface; and (3) a quadrilateral structured mesh with random distortion within the entire domain.

DOI: 10.1002/fld

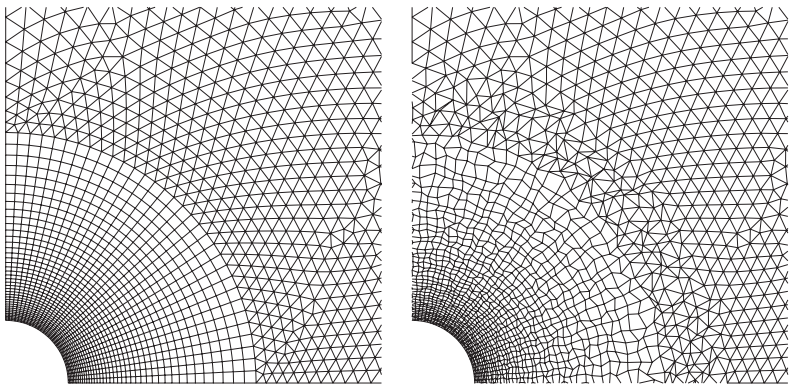

Figure 8. Mesh distortion of base hybrid mesh: (a) initial hybrid mesh; and (b) distorted hybrid mesh.

5.1. Flow around circular cylinder with mesh distortion

An initial quality hybrid mesh exterior to a circular cylinder was generated and then each node in an overlapping annular sub-region exterior to the circle was randomly moved by up to 50% of the local minimum edge length connected to the node. These two meshes are shown in Figure 8, and a close-up view of the two meshes near the mesh-type interface and corresponding nodedual and polygonal meshes are displayed in Figure 9. For an initial primal mesh, both the node-dual and polygonal control volume show almost identical control-volume shape. For the distorted case, a node-dual scheme results in non-convex finite-volumes in addition to the deviation of nodal location from the node-dual centroid because the variable is stored at the nodes of the primal mesh. However, the polygonal mesh still has convex control volumes and a centric location of variables because the scheme is not restricted by the nodal location of the primal mesh.

The deterioration in quality of the primal mesh due to node perturbation is mitigated by the structure of the polygonal mesh. Consequently, we see that the effect of distortion on the node-based dual control-volume mesh is more significant than in the polygonal case.

Node-dual and polygonal finite-volume schemes have been compared on their respective control-volume meshes for viscous flow about an impulsively started cylinder with $Re = 150$. The pressure fields at two different times during the evolving flow are compared in Figure 10.

While the pressure fields are qualitatively similar, we see that there are more pronounced oscillations with the node-dual scheme. These oscillations are evident in the contours of Figure 10. Since the graphics are processed on the same distorted meshes, the oscillations are not introduced by the graphics procedures.

Hydrodynamic forces exerted on the cylinder obtained by node-dual and polygonal schemes are compared in Figure 11. In contrast to the clear difference of the pressure fields presented in Figure 10, the drag and lift history show almost identical result for both node-dual and polygonal schemes. This result was expected because the force exerted on the cylinder is not a local quantity but instead is an the integrated quantity over the surface of the cylinder. Hence, even though there are pressure oscillations near the cylinder, the integrated quantity does not reveal this local oscillation. Nevertheless, a small decrease in C_D and C_L amplitudes can be observed for the

DOI: 10.1002/fld

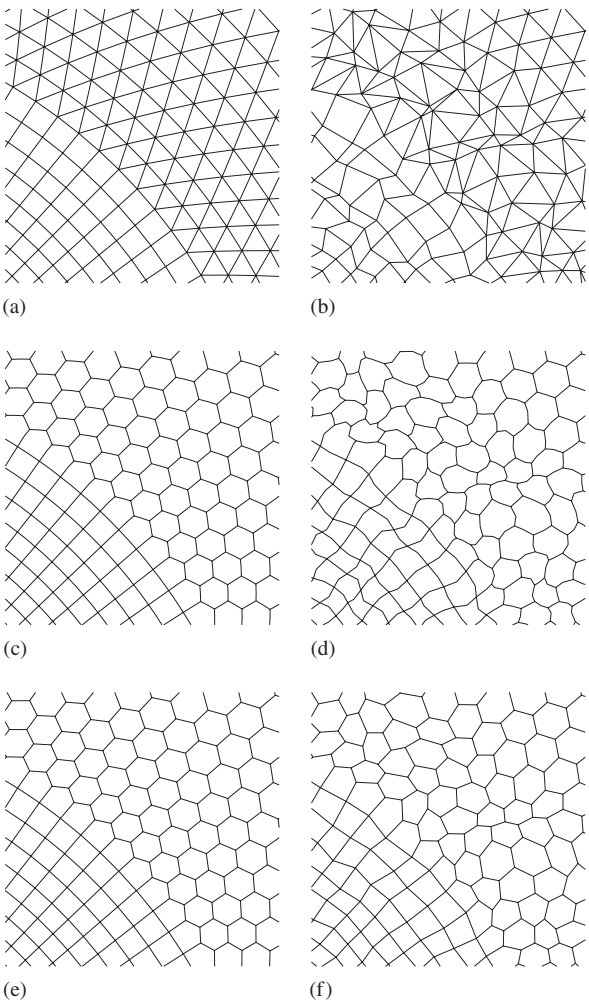

Figure 9. Mesh distortion effect on node-dual and polygonal control-volume construction: (a) initial hybrid mesh; (b) distorted hybrid mesh; (c) initial node-dual mesh; (d) distorted node-dual mesh; (e) initial polygonal mesh; and (f) distorted polygonal mesh.

node-dual scheme as compared to the polygonal scheme. This can be attributed to the additional dissipation introduced by a node-dual scheme on poor quality distorted meshes.

5.2. Discontinuous transition of element size

In the next test we consider the effect of a sudden change in mesh size at the interface of mesh subregions of different element shapes (triangle and quadrilateral). This is particularly relevant in certain viscous flow problems where an anisotropic structured mesh of slender quadrilaterals is desirable to capture a boundary layer zone near a wall and a transition to an unstructured mesh of triangles is desired in the far field.

DOI: 10.1002/fld

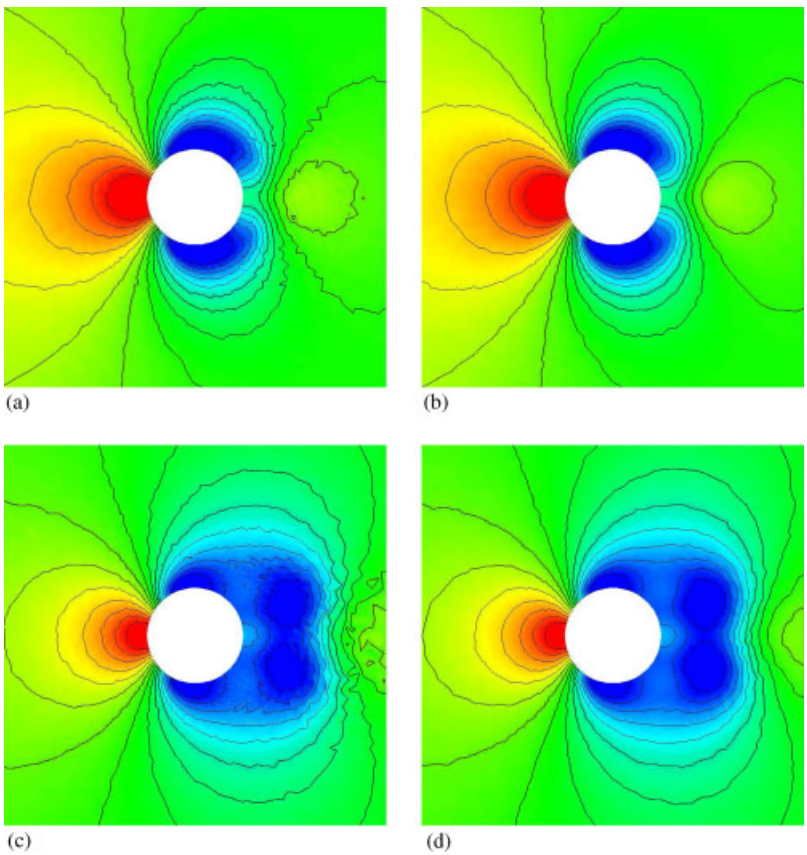

Figure 10. Comparisons of pressure fields obtained by node-dual and polygonal schemes on distorted hybrid mesh ($Re = 150$): (a) node-dual scheme at $t = 0.1D/U_\infty$; (b) polygonal scheme at $t = 0.1D/U_\infty$; (c) node-dual scheme at $t = 0.3D/U_\infty$; and (d) polygonal scheme at $t = 0.3D/U_\infty$.

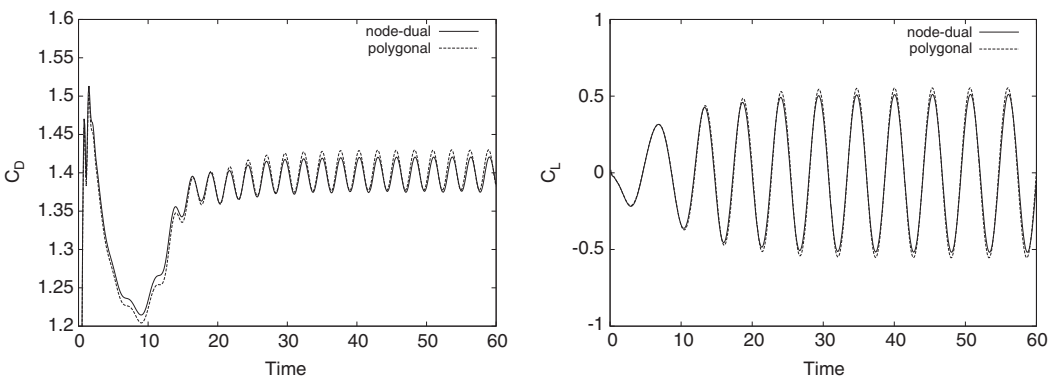

Figure 11. Comparison of hydrodynamic forces exerted on cylinder computed from node-dual and polygonal schemes on distorted hybrid mesh.

DOI: 10.1002/fld

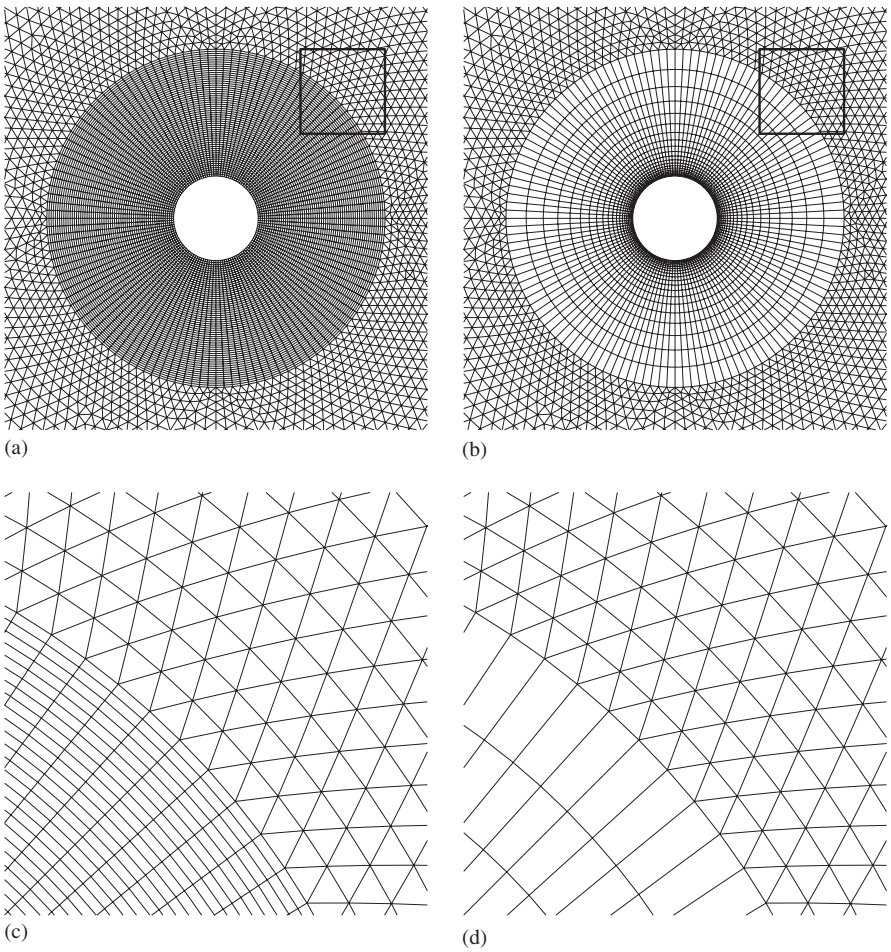

Figure 12. Irregular transitions of cell size at interface of hybrid mesh. Type 1 represents very thin quadrilaterals with long sides attached to isotropic triangles and type 2 represents very tall quadrilaterals with short bases touching the isotropic triangles. The triangular mesh is the same for both cases, but the inner quadrilateral region is different: (a) irregular transition type 1; (b) irregular transition type 2; (c) type 1 close-up; and (d) type 2 close-up.

The meshes for our test comparison are shown in Figure 12. The outer triangular mesh is fixed and the inner quadrilateral meshes in the two figures are, respectively, clustered and stretched near the interface. That is we have abrupt transitions in the radial direction to slender quadrilaterals and elongated quadrilaterals, respectively. The effect of these abrupt hybrid mesh transitions for the previous viscous flow problem is compared for node-dual and polygonal mesh schemes in Figure 13. For both types of irregular transitions, node-dual scheme exhibits strong pressure oscillations at the interface of the hybrid meshes. This effect is mitigated in the case of type 1 irregularity and negligible in type 2 irregularity, further confirming the robustness of the polygonal scheme over the conventional node-dual scheme.

DOI: 10.1002/fld

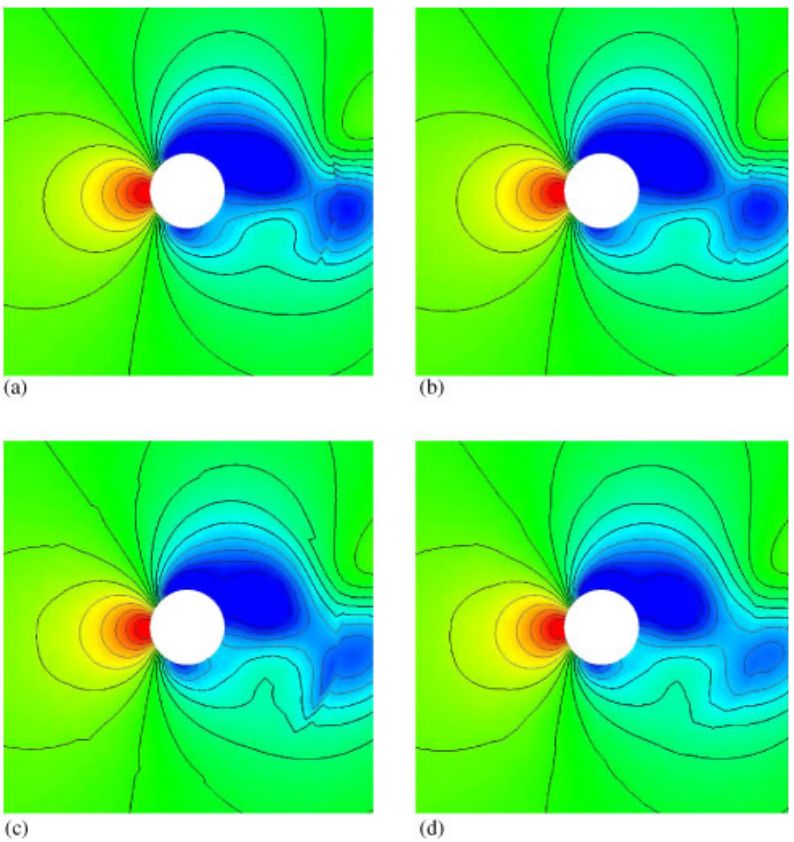

Figure 13. Comparisons of node-dual and polygonal schemes on different types of irregular mesh transitions in hybrid meshes. Pressure fields are captured approximately at the same time step within a shedding cycle: (a) type 1 with node-dual; (b) type 1 with polygonal; (c) type 2 with node-dual; and (d) type 2 with polygonal.

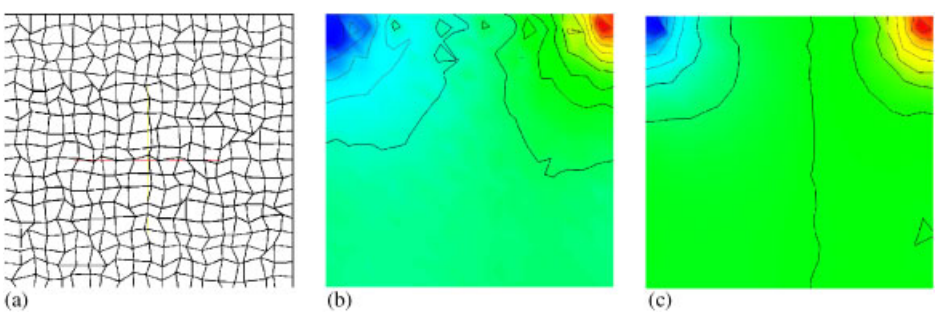

Figure 14. Comparison of node-dual and polygonal methods for lid-driven cavity problem on randomly distorted mesh ($Re = 10$): (a) 20×20 structured mesh with random distortion; (b) pressure field from node-dual scheme; and (c) pressure field from polygonal scheme.

DOI: 10.1002/fld

5.3. Lid-driven cavity problem with mesh distortion

As a final test problem to demonstrate the robustness of the polygonal scheme over the node-dual scheme, the familiar lid-driven cavity problem is considered discretised with a 20×20 structured quadrilateral base mesh. This initial mesh is randomly perturbed by up to 50% of the local edge length as before to represent mesh quality degradation. The distorted mesh is shown in Figure 14(a). Pressure fields computed from node-dual and polygonal schemes using the distorted mesh are compared in Figure 14(b) and (c). As in the previous case, the node-dual scheme exhibits severe oscillation in the pressure field while the polygonal scheme has a more stable solution.

6. CONCLUSION

The node-dual finite-volume scheme is sensitive to mesh distortion and we propose an alternative polygonal finite-volume scheme to promote more robust calculations on unstructured hybrid meshes. The schemes are compared for viscous flow test problems using hybrid meshes in 2D. The results for test cases with randomly perturbed node locations in an annular subregion adjacent to a impulsively started cylinder reveal smoother pressure contours in the case of the polygonal control-volume scheme. The node-dual scheme has numerous oscillations induced by the mesh perturbations and these are exacerbated where there is a transition from triangles to quadrilaterals. This latter point is taken up in a subsequent test which indicates that the polygonal scheme is less sensitive to abrupt changes in mesh size at an interface between two different mesh types. Some additional numerical application studies are given in [16, 18]. The effectiveness of the present polygonal scheme is not limited to incompressible flow test problem but can be expected to be valid in compressible regimes and also other flow and transport problems including convection and diffusion processes. More detailed studies are warranted but the present work clearly displays the effects of unstructured hybrid meshes and the need to preserve smoothly graded schemes. The study suggests that the polygonal approach is superior in practical applications where irregular unstructured meshes are the norm. Future work will include the extension to 3D arbitrary polyhedral meshes using the 3D construction described here.

A more mathematical analysis is also needed to provide a rigorous understanding of the improved behaviour in the polygonal scheme. We conjecture that such an analysis might be similar to that used in finite element analysis where distortion of cells in the physical domain is directly related to the Jacobian of the transformation to a regular cell in a reference domain. The map and its inverse enter in the error bounds for finite elements [29, 30], so the better shaped cell with the polygon approach would imply a better map and therefore a better constant in the error estimate (albeit the same asymptotic rate). Likewise the effect of the respective cell choices on solution iterations and conditioning is also of interest and an approach similar to that in the mesh of mesh quality studies of Branets and Carey [3, 4] may be relevant.

REFERENCES

1. Athanasiadis AN, Deconinck H. Object-oriented three-dimensional hybrid grid generation. *International Journal for Numerical Methods in Engineering* 2003; **58**:301–318.
2. Carey GF. *Computational Grids*: *Generations*, *Adaptation and Solution Strategies*. Taylor & Francis: London, 1997.
3. Branets L, Carey GF. A local cell quality metric and variational grid smoothing algorithm. *Engineering with Computers* 2005; **21**:19–28.

DOI: 10.1002/fld

4. Branets L, Carey GF. Extension of a mesh quality metric for elements with a curved boundary edge or surface. *Journal of Computing and Information Science in Engineering* 2005; **5**:302–308.
5. Knupp P. Algebraic mesh quality metrics. *SIAM Journal on Scientific Computing* 2001; **23**:193–218.
6. Wright JA, Smith RW. An edge-based method for the incompressible Navier–Stokes equations on polygonal meshes. *Journal of Computational Physics* 2001; **169**:24–43.
7. Loubère R, Shashkov MJ. A subcell remapping method on staggered polygonal grids for arbitrary-Lagrangian–Eulerian methods. *Journal of Computational Physics* 2005; **209**:105–138.
8. Belov A, Jameson A, Martinelli L. A new implicit algorithm with multigrid for unsteady incompressible flow calculations. *AIAA Paper 95-0049*, 1995.
9. Jameson A. Time-dependent calculations using with applications to unsteady flows past airfoils and wings. *AIAA Paper 91-1596*, 1991.
10. Turkel E. Preconditioned method for solving the incompressible and low speed compressible equations. *Journal of Computational Physics* 1987; **72**:277–298.
11. Turkel E. A review of preconditioning methods for fluid dynamics. *Applied Numerical Mathematics* 1993; **12**:257–284.
12. Malan AG, Lewis RW, Nithiarasu P. An improved unsteady, unstructured, artificial compressibility, finite-volume scheme for viscous incompressible flows. Part I. Theory and implementation. *International Journal for Numerical Methods in Engineering* 2002; **54**:697–714.
13. Nithiarasu P. An efficient artificial compressibility (ac) scheme based on the characteristic based split (cbs) method for incompressible flows. *International Journal for Numerical Methods in Engineering* 2003; **56**:1815–1845.
14. Lin PT. Two-dimensional implicit time dependent calculation for incompressible flows on adaptive unstructured meshes. *Ph.D. Thesis*, Princeton University, Princeton, 2001.
15. Turkel E. *Preconditioning and the Limit of the Compressible to the Incompressible Flow Equations for Finite Difference Schemes in the Frontiers of the Computational Fluid Dynamics 1994*, Chapter 13. Wiley: New York, 1998.
16. Kallinderis Y, Ahn HT. Incompressible Navier–Stokes method with general hybrid meshes. *Journal of Computational Physics* 2005; **210**:75–108.
17. Barth TJ. Aspects of unstructured grids and finite-volume solvers for the Euler and Navier–Strokes equations. Unstructured grid methods for advection dominated flows. *Technical Report AGARD Report 787*, AGARD, 1992; 6.1–6.60.
18. Ahn HT. A new incompressible Navier–Stokes method with general hybrid meshes and its application to flow/structure interactions. *Ph.D. Thesis*, The University of Texas at Austin, TX, 2005.
19. Roe PL. Approximate Riemann solvers, parameter vectors and difference schemes. *Journal of Computational Physics* 1981; **43**:357–372.
20. Taylor LK, Whitfield DL. Unsteady three-dimensional incompressible Euler and Navier–Stokes solver for stationary and dynamic grids. *AIAA* 1991; **92**:1650.
21. Anderson WK, Rausch RD, Bonhaus DL. Implicit/multigrid algorithms for incompressible turbulent flows on unstructured grids. *Journal of Computational Physics* 1996; **128**:391–408.
22. Kim S. Reynolds-averaged Navier–Stokes computation of tip clearance flow in a compressor cascade using an unstructured grid. *Ph.D. Thesis*, Virginia Polytechnic Institute and State University, 2001.
23. Anderson WK, Bonhaus DL. Algorithm for computing turbulent flows on unstructured grids. *Computers and Fluids* 1994; **23**:1–21.
24. Haselbacher A, Blazek J. On the accurate and efficient discretization of the Navier–Stokes equations on mixed grids. *AIAA Journal* 2000; **38**:2094–2102.
25. Chen AJ, Kallinderis Y. Adaptive hybrid (prismatic-tetrahedral) grids for incompressible flows. *International Journal for Numerical Methods in Fluids* 1998; **26**:1085–1105.
26. Braaten ME, Connell SD. Three-dimensional unstructured adaptive multigrid scheme for the Navier–Stokes equations. *AIAA Journal* 1996; **34**:281–290.
27. Venkatakrishnan V, Allmaras S, Kamenetskii D, Johnson F. Higher order schemes for the compressible Navier–Stokes equations. *AIAA Paper 2003-3987*, 2003.
28. Ahn HT, Kallinderis Y. Strongly coupled flow/structure interactions with a geometrically conservative ALE scheme on general hybrid meshes. *Journal of Computational Physics* 2006; **219**:671–696.
29. Carey GF, Oden JT. *Finite Elements*: *A Second Course*. vol. II. Prentice-Hall: Englewood Cliffs, NJ, 1983.
30. Carey GF, Oden JT. *Finite Elements*: *Mathematical Aspects*. vol. IV. Prentice-Hall: Englewood Cliffs, NJ, 1983.

DOI: 10.1002/fld